

On electron betatron motion and electron injection in laser wakefield accelerators

This content has been downloaded from IOPscience. Please scroll down to see the full text.

2014 Plasma Phys. Control. Fusion 56 084009

(<http://iopscience.iop.org/0741-3335/56/8/084009>)

View [the table of contents for this issue](#), or go to the [journal homepage](#) for more

Download details:

IP Address: 141.213.19.93

This content was downloaded on 09/12/2014 at 20:25

Please note that [terms and conditions apply](#).

On electron betatron motion and electron injection in laser wakefield accelerators

T Matsuoka¹, C McGuffey², P G Cummings, S S Bulanov³, V Chvykov,
F Dollar⁴, Y Horovitz⁵, G Kalintchenko, K Krushelnick, P Rousseau⁶,
A G R Thomas, V Yanovsky and A Maksimchuk

Center for Ultrafast Optical Science, University of Michigan, Ann Arbor, Michigan 48109-2099, USA

E-mail: agrt@umich.edu

Received 2 December 2013, revised 6 May 2014

Accepted for publication 22 May 2014

Published 22 July 2014

Abstract

We performed laser wakefield electron acceleration experiments using laser powers up to 100 TW in the ‘bubble’ regime. The measured angularly resolved energy spectra of the electron beam showed evidence of betatron oscillations during the acceleration process. Through diagnosis of these oscillations, electron injection into the wakefield could be controlled through adjustment of the shape of the laser focal spot or through changes in the plasma density. Several different acceleration regimes could be accessed including (i) injection of a single electron bunch into the wakefield ‘bubble’ (ii) multiple injection of several electron bunches and/or (iii) production of a transverse break up of the electron beam within the ‘bubble’ due to an asymmetry of the wakefield. We apply analytical formulae for electron motion in a wakefield to understand the experimental data.

Keywords: laser, plasma, accelerators, wakefield, betatron

(Some figures may appear in colour only in the online journal)

1. Introduction

Laser wakefield electron accelerators (LWFAs) [1–9] are a potentially attractive ultra-short pulse source of electrons and x-rays for scientific and medical applications [10–12] due to their compact size. In previous work, narrow divergence synchrotron-like x-ray beams have been obtained from LWFA experiments up to energies of a few 10 s of keV having a peak brightness comparable to that of 3rd generation synchrotron sources [13–22]. In LWFA x-ray sources, laser generated relativistic plasma waves in a low density plasma are used as the medium for generation and acceleration of an electron beam. The same plasma also provides a ‘wiggler’ [13, 20, 21, 23] for x-ray production because of the transverse electric fields

in the accelerating plasma wave structure. In this plasma wiggler, electrons in the beam execute transverse oscillations (orthogonal to the direction of electron beam propagation) as they are accelerated consequently producing x-rays. The x-ray spectrum has previously been characterized as having a synchrotron-like shape with a peak at the critical energy given by

$$E_c = \frac{3}{4} \gamma^2 \hbar \omega_p^2 \frac{r_\beta}{c},$$

where γ is the Lorentz factor of electron beam, ω_p is the plasma frequency in the ambient plasma and r_β is the betatron oscillation amplitude in the plasma cavity [24]. Understanding the underlying dependence of the oscillations on experimentally controllable parameters such as plasma density, laser intensity, pulse shape and interaction length is necessary for the development of a reliable x-ray source [25–27].

In this paper, we investigate how electron injection mechanisms for laser wakefield acceleration can be controlled and show that measurements of angularly resolved electron spectra can be used to retrieve the electron trajectories in the

¹ Present address: Photon Pioneers Center in Osaka University, Techno-Alliance Building Rm. A807, 2-8 Yamadaoka, Suita, Osaka, 565-0871, Japan.

² Present address: University of California, San Diego, CA 92093, USA.

³ Present address: University of California, Berkeley, CA 94720, USA.

⁴ Present address: Dynamical Experiments Group, Propulsion Division, Soreq NRC, Yavnee 81800, Israel.

⁵ Present address: JILA, University of Colorado, Boulder, CO 80309, USA.

⁶ Present address: LOA, Ecole Polytechnique, Paris, France.

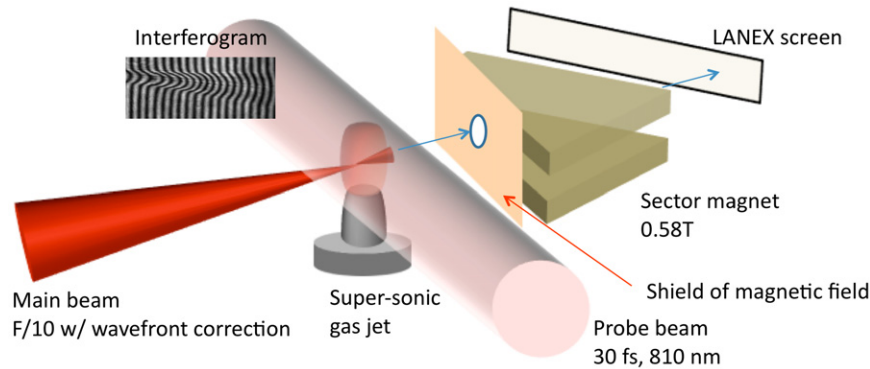


Figure 1. Experimental setup.

bubble shaped wakefield [28, 29] to determine the injection process. It was possible to access several regimes of acceleration in these experiments: (i) single beam injection when the bunch charge was small (ii) multiple consecutive injection events of electron bunches into the wakefield (resulting in a significant increase in total beam charge from beam driven acceleration) (iii) single beam injection at higher current, resulting in break up of the beam within the bubble due to asymmetries in the wakefield. The generation of such beams may also lead to enhanced x-ray production. For applications, control of the injection and instability processes during wakefield acceleration in the bubble regime is critical.

We also show that analytical formulae for electron motion in a bubble-shaped wakefield show reasonable agreement when compared with the experimental data. This data consequently provides useful information about the interaction of the electron beam with the laser generated wakefield. The only free parameter in the model is the radius of the bubble (r_b), which was found to be close to the matched spot size for self focusing $r_b = 2\sqrt{a_0}c/\omega_p$ [30], where $a_0 = eE_0/mc\omega_0$ is the normalized vector potential of the laser.

2. Experimental results

In the experiments, (figure 1) a high power laser pulse ($\lambda_0 = 800$ nm, $\tau = 35$ fs) irradiated a helium or hydrogen gas jet target. No significant difference between helium and hydrogen was observed for our experiments. Two standard conical supersonic gas jets [31] of diameters 2 and 5 mm were used in the experiments discussed here.

Using an $f/10$ configuration, the 10 cm diameter laser beam was focused using a 1 m focal length off-axis parabolic mirror to a spot of $10 \mu\text{m}$ full-width-at-half-maximum (FWHM) containing 60% of the pulse energy, after wavefront correction with a deformable mirror [32]. A peak focused intensity of $I = 8 \times 10^{19} \text{ Wcm}^{-2}$ was achieved when using a laser power of 100 TW.

A probe pulse was generated by splitting 4% from the interaction pulse using a $2 \mu\text{m}$ thick pellicle and sent through the plasma, orthogonally to the interaction pulse, as a diagnostic beam. A shearing interferometer was used in the probe arm to measure the plasma density profile with a 12-bit charge coupled device (CCD) camera as the detector. The

spatial resolution for these measurements was approximately $10 \mu\text{m}$. An interference filter with a central wavelength of 800 nm and a bandwidth of 100 nm was placed in front of the CCD. Accelerated electrons produced in the interaction were deflected by a sector shaped magnet and were measured by a LANEX (Kodak) scintillating screen. In some experiments, the magnet was replaced by a square magnet to improve energy resolution. The front surface of the LANEX screen was shielded to block light emission from the plasma as well as electrons with energies below 80 keV. Light emitted by the LANEX screen was imaged by a lens onto another CCD camera through a BG-39 (Schott Glass) filter. The detection energy range of the spectrometer with the sector (square) magnet was between 14 and 200 (40 and 350) MeV. The energy scale on the LANEX screen is nonlinear and hence the resolution was ± 5 (or ± 1) MeV for 50 MeV electrons, and ± 7 (or ± 2) MeV for 100 MeV, which was limited by a typical electron beam divergence of 10 mrad. The camera signal was absolutely calibrated to the charge by use of an imaging plate [33]. The transmitted laser beam was also reflected by a glass wedge and then re-imaged in order to measure the laser mode and spectrum.

Angularly resolved electron energy spectra are shown in figure 2. The vertical axis is perpendicular to the polarization plane of the laser and represents the angular distribution of electrons. The horizontal axis represents the electron kinetic energy. Electron bunch charge is shown in the right corner of each image and was obtained by integrating signal in the whole image.

The spectra indicate a threshold plasma density for the generation of trapped electrons, as seen by other authors [34]. We observed that the difference between electron bunch charge below and above the injection threshold at fixed laser power was about one order of magnitude [39]. In these experiments, the threshold density for 80 (30) TW was $n_e = 1.3 \times 10^{19} \text{ cm}^{-3}$ ($n_e = 1.7 \times 10^{19} \text{ cm}^{-3}$). When the laser pulse (focused to $a_0 = 3$) irradiated the plasma below the threshold density, as in figure 2(a), a single bunch with a narrow angular width was consistently observed and the measured shot-to-shot fluctuations (beam pointing, spectral shape) were small. Here we use a_0 as that corresponding to the *peak* intensity at focus in vacuum. In this case, the energy spectrum observed is quasi-monoenergetic indicating a combination of electron beam injection stopping and phase rotation.

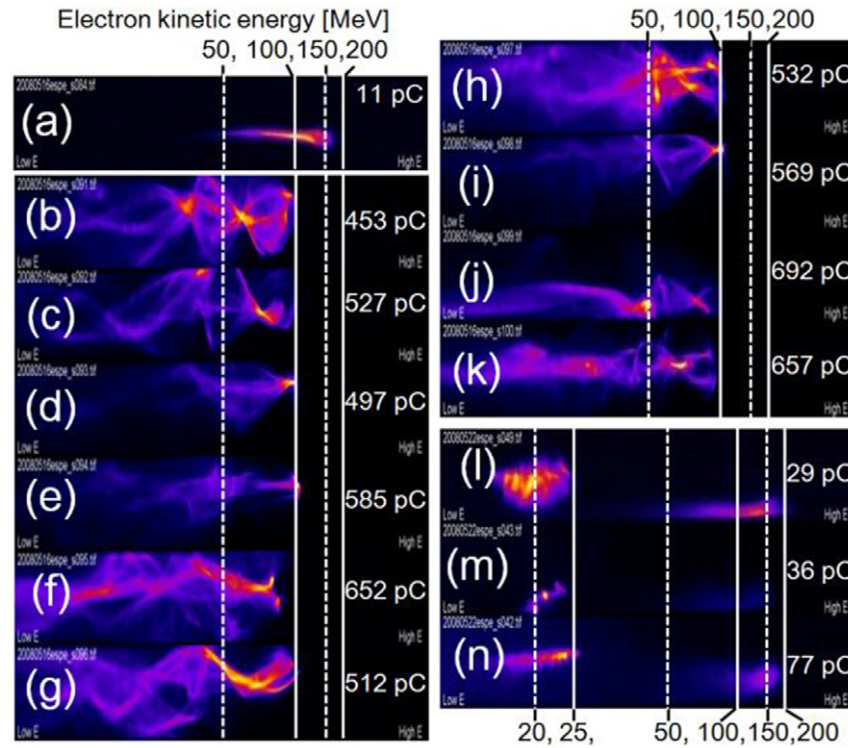


Figure 2. Angularly resolved electron spectra from a He gas jet. The vertical axis is the angle of an electron propagating in a straight line from a point at the gas jet exit and the horizontal axis shows the electron kinetic energy. Plasma density is (a) $n_e = 1.2 \times 10^{19} \text{ cm}^{-3}$, (b)–(k) $n_e = 1.8 \times 10^{19} \text{ cm}^{-3}$, and (l)–(n) $n_e = 1.0 \times 10^{19} \text{ cm}^{-3}$, respectively. Numbers within individual images indicate the total electron charge. Laser intensity was in the range of (a)–(k) $a_0 = 3.0$ – 3.3 corresponding to a power of 30 TW and (l)–(n) $a_0 = 5.1$ – 5.4 corresponding power of 80 TW.

When the plasma density was increased above the threshold, the charge increased dramatically (in excess of 50 \times) and the measured beam divergence increases significantly. The energy spectrum becomes broad and generally shows multiple traces of betatron oscillations along energy axis. (i.e., different beam energies are emitted with slightly different emission angles which is evident in the measurement of emission angle versus electron energy in figure 2). Individual traces clearly indicate continuous injection into the first bubble. Observation of multiple traces suggests that either that breakup of the single bunch or multiple bunch injection occurs within the bubble. Ten consecutive shots with identical parameters are shown in figures 2(b)–(k) also demonstrating significant fluctuations in this regime.

More than half of the shots show clear transverse oscillations i.e., (b), (c), (f)–(h), (i), (k), and often (b), (k) show separate correlated traces due to multiple bunches which co-propagate (for example, two bunches which move side by side together) in the first bubble. Similar multiple bunches are observed in 2D particle-in-cell simulations [35], in which a laser beam with an intensity profile asymmetry splits into two laser filaments propagating side by side. Each of the laser filaments produces a bubble and therefore accelerate electron bunches propagating side by side. (b) and (k) are similar to this ideal 2D case. However, since this trajectory is sensitive to the initial transverse momentum and position at the moment of the injection, small asymmetries can cause non-symmetric oscillation patterns and significant shot to shot

fluctuations. The main reason that the betatron oscillations can be so clearly observed in these experiments is due to intensity profile asymmetries of the laser pulse and consequently of the bubble-shaped plasma wakefield [25, 36–38].

When a higher intensity, more symmetric laser-pulse (with $a_0 = 5$) irradiated a plasma above the threshold density, a second electron bunch with higher charge at electron energy of $E < 50$ MeV appeared consistently. Such a second bunch could be generated by a subsequent injection in same bubble as the first bunch but at a later time, such that acceleration time is shorter and hence results in a lower energy electron bunch. The time interval between injection of the first and second bunches is determined by beam loading of the first bunch. It is unlikely that injection in a second bubble behind the first one was occurring since the amplitude of this part of the plasma wakefield is typically much smaller due to turbulence of the plasma (i.e., subsequent plasma waves are not driven to the wave breaking in this regime).

We found necessary conditions for experimental observations of transverse oscillations in our electron beam diagnostic to be continuous injection of electrons at a particular point in the wakefield and an acceleration length less than the dephasing length but long enough for the beam to undergo more than one betatron oscillation. When the acceleration length is longer than the dephasing length, phase rotation of the electron bunch mixes the accelerating and decelerating phases of the bunch and, therefore, the experimental trace becomes too complex to extract useful information.

3. Discussion

To interpret the oscillations observed in these spectra we used simple analytical models demonstrating that the oscillation amplitude of the electron trajectory could be retrieved. We compared two models in the literature, a constant longitudinal field betatron model [36] and a ‘bubbletron’ model [43]. The constant field betatron model had been shown to reproduce angularly resolved electron spectrum from experiments, however this uses an unrealistic assumption that the longitudinal acceleration field is constant. In our experiments the acceleration was rather in the ‘blowout’ or ‘bubble’ regime [28–30]. In our measurements, the electron energy is reasonably well reproduced by the scaling in [30]. We have also previously obtained experimental evidence of the bubble structure [41]. We used a test particle model (‘bubbletron’) that calculates electron trajectories in the non-evolving bubble with the initial conditions of an electron beam according to [43]. In the ‘bubbletron’, a spherical ion cavity (bubble) is assumed. The bubble of a constant radius r_b moves at a velocity of v_b in the x direction. We used the nonlinear phase velocity given by $v_b/c = 1 - (3/2)\omega_p^2/\omega_0^2$ in the blowout model [44]. The equation of motion of a test particle (a single electron) in the bubble yields [42, 29]

$$\frac{d\mathbf{p}}{dt} = -\frac{m\omega_p^2}{2}\mathbf{r},$$

where $\mathbf{r} = \xi\hat{x} + y\hat{y} + z\hat{z}$. Here, a frame co-moving with the bubble (bubble frame): $\xi = x - v_b t$ is used with laboratory frame time t . The solution of electron momenta are obtained as [42]

$$p_x = \frac{m\omega_p^2\gamma_b^2}{2c} (r_b^2 - \xi^2),$$

$$p_y = \left(\frac{p_x}{\gamma_0}\right)^{1/4} \sqrt{p_{y0}^2 + \frac{m^2\omega_p^2\gamma_b^2}{2}}$$

$$\times \cos \left[2\gamma_p \left(\arcsin \left(\frac{ct}{2r_b\gamma_b^2} \right) + \frac{\pi}{2} \right) \right].$$

Here, γ_0 is the electron beam Lorentz factor and $\gamma_b = 1/\sqrt{1 - v_b^2/c^2}$ is the Lorentz factor associated with the bubble. We set $\xi = 0$ at the center of the bubble. ξ can be calculated based on an approximation made here i.e., $x \simeq ct$ and yields $\xi \simeq ct/2\gamma_b^2$. The initial transverse momentum and transverse coordinate of the electron are p_{y0} and y_0 respectively. In the spherical bubble, axial symmetry implies an injection point at $y_0 = 0$ and the transverse momentum to be $p_{y0} = \pi a_0 mc/4$ [43]. The initial electron energy becomes $\gamma_0 = \gamma_b \sqrt{1 + p_{y0}^2/m^2c^2}$. The output angle from the ion channel cavity can be estimated by $\theta \simeq p_y/p_x$ with the use of the above equations. The parameters for the bubbletron model are r_b , ω_p and a_0 . The bubble radius is set at matched spot radius $r_b = 2\sqrt{a_0}c/\omega_p$ for guided propagation [30].

The experimentally measured electron density from interferometer data was used to estimate ω_p . Since the laser intensity is unknown in the plasma due to self focusing, a_0 was adjusted to fit the observed betatron period. We define

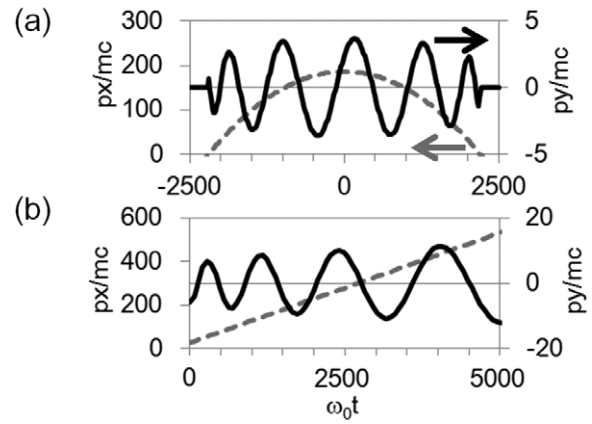


Figure 3. Electron momenta shown as a function of time ($\omega_0 t$) for (a) bubbletron and (b) betatron motion, respectively. Dashed line is p_x and solid line is p_y . Plasma density is set at $n_e = 1.8 \times 10^{19} \text{ cm}^{-3}$. Parameters are, for bubbletron motion, $a_0 = 2.8$, for betatron, $E_x = m\omega_p c/e$, $\gamma_0 = 4$, and $y_0 = 4.5 \mu\text{m}$.

the adjusted a_0 as a_{0d} . The adjusted intensity is typically slightly ($\sim 10\%$) lower than that of the vacuum focus. This is consistent with the a_0 estimated from the relativistic red shift of stimulated Raman side scattering in our experiments [45]. Comparative results are shown in figures 4(a), (b) as the image from experiments, solid curve, dashed–dotted curve (bubbletron model) and dashed curve (betatron model). Data is displayed which show transverse oscillations having a peak energy close to the dephasing limit, since ideal results can be obtained only for situations where the bubble has a precisely spherical shape. For the betatron model, the longitudinal constant acceleration field E_x , initial electron energy γ_0 , and initial transverse offset y_0 are adjusted to obtain a best fit to the image by use of [36].

It is clear that the bubbletron should be a better fit to the data than the constant field betatron model, since there is no limitation on maximum electron energy in this simple theory. On the other hand, the bubbletron model shows a cut off at high electron energy. This can be seen in figures 3(a) and (b) where electron momenta are shown as a function of time for both models. In the constant field betatron model, the electron bunch gains energy continuously since the accelerating field is constant along x . In the bubbletron model, electrons gain energy until they reach the center of the bubble ($\omega_0 t = 0$) after which they lose energy. When the electron reaches the front of the bubble ($\omega_0 t \approx 2000$), the electron eventually moves backwards (relative to the bubble). This phenomenon is due to the parabolic shape of the bubble potential, however, in most cases the laser will deplete before this can occur. The cut off and the oscillation period consequently depends on r_b while the amplitude is dependent on p_{y0} .

The bubbletron model underestimates the amplitude in figure 4(b) (solid curve) but correctly reproduces the trajectory for figure 4(c). The bubble radius $r_b = 6.9 \mu\text{m}$ is larger than that in figure 4(a) ($r_b = 4.3 \mu\text{m}$) due to the larger a_0 and the smaller plasma frequency. The charge of the bunch may also affect the trajectory. When p_{y0} is increased to 8.0, the outermost trace in figure 4(b) is well reproduced by the bubbletron model as shown by the dotted–dashed curve. The

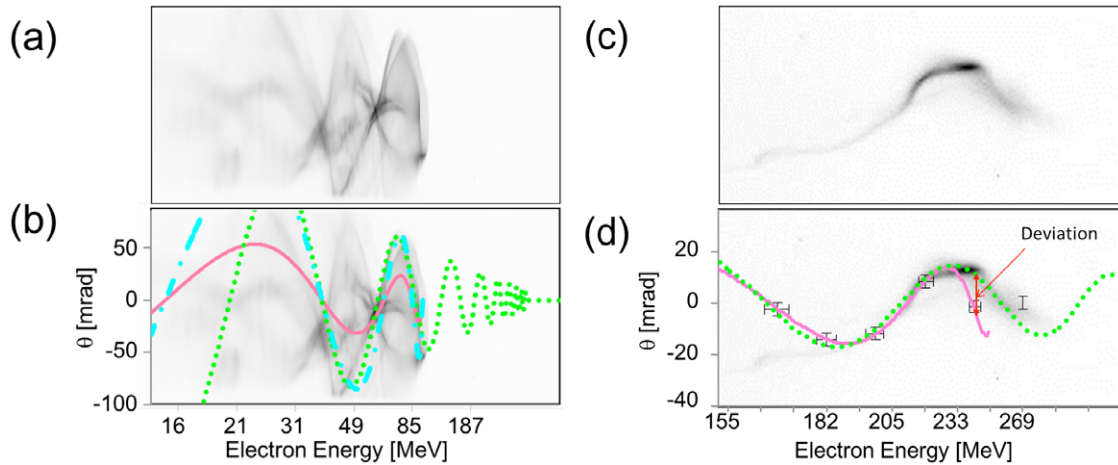


Figure 4. Angularly resolved electron spectra. (a) The gray scale image from figure 2(b). (b) Same image is overlaid with the theoretical trajectory of electrons from the bubbletron (solid curve with $p_{y0}/mc = \pi a_{0d}/4 = 2.2$, dashed-dotted curve with $p_{y0}/mc = 8.0$) and constant field betatron (dashed line) motion. Experimental parameters are $n_e = 1.8 \times 10^{19} \text{ cm}^{-3}$, gas jet nozzle diameter of 2 mm and $a_0 = 3.0$. Other parameters are; for the bubbletron curve, $a_{0d} = 2.8$; for constant field betatron, $E_x = m\omega_p c/e$, $\gamma_0 = 4$, and $y_0 = 4.5 \mu\text{m}$. (c) Is an image with high laser intensity ($a_0 = 4.4$) and long gas jet nozzle (5 mm) (not shown in figure 2). This integrated charge is 1400 pC. (d) Same image overlaid with theoretical curves. The solid curve is for the bubbletron with $p_{y0}/mc = a_{0d}/4 = 3.5$, dashed line for betatron. Experimental parameters are $n_e = 1.1 \times 10^{19} \text{ cm}^{-3}$, gas jet nozzle diameter of 5 mm and $a_0 = 4.4$. For the bubbletron curve, $a_{0d} = 4.4$, for the constant field betatron, $E_x = m\omega_p c/e$, $\gamma_0 = 6$, and $y_0 = 3 \mu\text{m}$.

oscillation amplitude is approximately equal to the bubble diameter for $p_{y0} = 8.0$ thus the outermost trace represents electrons moving at the edge of the bubble. The sensitivity of r_b for the fitting is shown in figure 5. The curve deviates from experimental data when the r_b is changed more than 5% from the best fit results ($a_{0d} = 2.8$ for figure 5(b), $a_{0d} = 4.4$ for figure 5(d)). Uncertainty of r_b is less than $\pm 0.3 \mu\text{m}$ for 5(a) and $\pm 0.2 \mu\text{m}$ for 5(c), respectively.

It is remarkable that the single parameter a_0 can fit both the high energy cut off and period as shown in figure 4(a). Consequently this suggests the validity of the bubbletron model in these experiments. The oscillation periods are reproduced well by the model. This shows that trajectories of the electrons after injection are dominated by the bubble shape (radius of the bubble), which is not sensitive to beam loading. The observation that the amplitude is not reproduced by the model indicates that the initial transverse momentum is sensitive to beam loading (i.e., collective effects from beam fields within the bubble). In figure 4(d), the deviation is clear in energy greater than 233 MeV. This deviation could be explained by the interaction between laser pulse and the electron bunch as reported in [47]. And this provides the evidence that the electron is accelerated in the first wake not from second wake.

The observed bunch charge is high enough such that beam loading can also change the longitudinal bubble shape if the bunch length is on the order of plasma wake period ($\tau_p = 2\pi/\omega_p$) [46]. The plasma wake period for figures 2(b)–(k) is 26 fs. The influence of beam loading can be measured by estimating the charge imbalance between bubble and electron bunch and is given by [40]

$$C = k_p^4 r_b^4 - 8\Gamma_0 k_p^2 r_t^2.$$

Here, electron bunch density is given by $\Gamma_0 = k_p^2 N_b / 2\pi n_p c \tau_p$, with total electron number in the bunch N_b . r_t is the radius of

the sheath of the bubble where the head of the electron bunch is and is taken to be r_b (i.e., maximum energy is achieved when the head of the electron bunch reaches the center of the bubble). We assumed electron beam duration to be $t_p = r_b/c$. By taking this duration, the electron beam fills the back half of the bubble. This assumption is consistent with dephasing of the electron beam and continuous injection. By substituting the parameters for figures 4(a), (c) yields $C = -340 \pm 20$, and $C = -1030 \pm 30$, respectively. Note that due to the uncertainty of the charge calibration, the lowest estimate of charge was used for figure 4(c). This means that the bubble is fully beam loaded in both cases. On the other hand, parameters for figure 2(a) yields $C = -7$ indicating in this case it is close to the beam loading threshold ($C = 0$). Therefore, it is clear from our data that transverse oscillations are significantly affected by beam loading.

It is unlikely that using the bubbletron model alone without consideration of beam loading can reproduce the experimental data accurately when the beam charge is high. Indeed bubble fields will be most influenced at the back of the electron bunch where electron energies are low rather than at the head of the bunch. Consequently, the model fails to reproduce the oscillation amplitude for figure 4(a) where multiple traces are observed indicating break up of the electron beam within the bubble. Note that the high energy end of the electron bunch could be distorted due to interactions with the laser pulse [47] when the electron beam is close to the dephasing ($\xi > r_b$). The deviation from the bubbletron model in figure 4(c) at above 230 MeV is likely due to complex interactions with the laser pulse.

The root mean square (RMS) beam divergence of the electron bunch above electron energy of 50 MeV is shown in figure 6 as a function of electron bunch charge. The parameters for data points are in the range of $n_e = 1.2\text{--}2.1(1.0) \times 10^{19} \text{ cm}^{-3}$ and $a_0 = 2.9\text{--}3.6(5.1)$ for 30 (80) TW points.

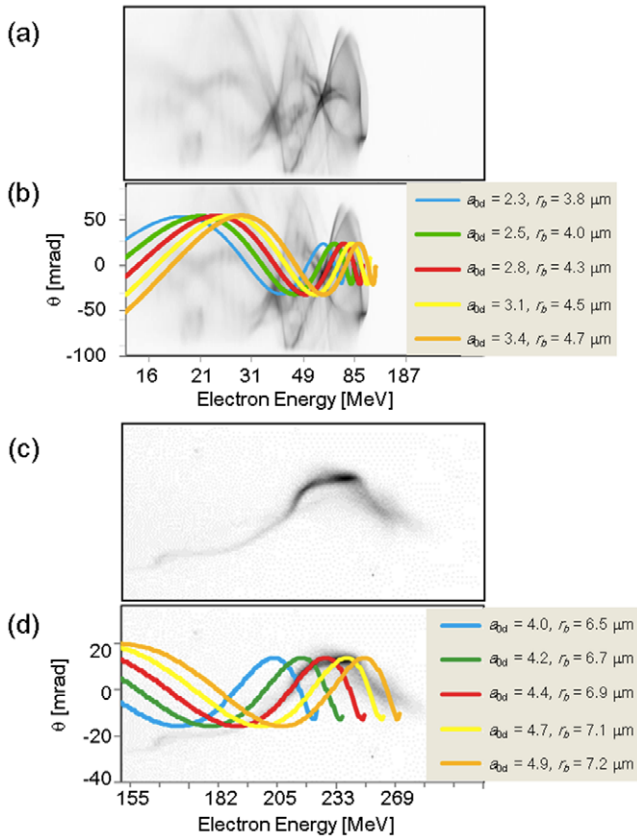


Figure 5. Sensitivity of a_{0d} to the electron trajectory. (a) The gray scale image from figure 4(a). (b) Same image is overlaid with theoretical trajectory of electrons from bubbletron model with variation of a_{0d} from 2.3 to 3.4. (c) The gray scale image from figure 4(c). (d) Same image is overlaid with theoretical trajectory of electrons from bubbletron model with variation of a_{0d} from 4.0 to 4.9. Other parameters are identical to the one in figure 4. a_{0d} and r_b are listed in the right of (c) and (d).

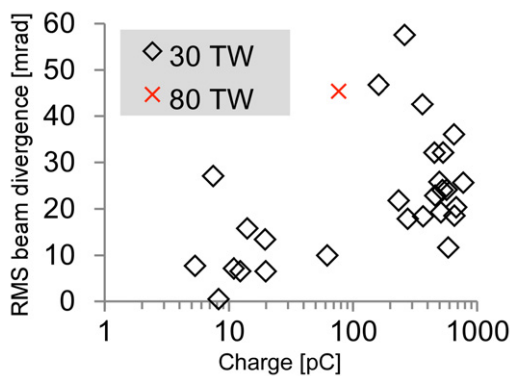


Figure 6. RMS beam divergence obtained from angularly resolved electron spectrum.

The beam divergence increases with bunch charge. This corresponds to the trend shown in the figure 2 indicating large transverse oscillation when the electron beam charge is large. Three factors could be considered to explain this effect. First, electrons could gain large transverse momentum at the moment of injection into the bubble when the injected charge is large which results in large transverse field at the injection point. This is similar to the results found in [27], where pulse front

tilt achieved a similar effect. Second, the electron bunch can modify the shape of the bubble as shown by particle-in-cell simulations [28] and phenomenological theory [40]. Third, bunch self generated fields can affect the trajectory of electrons which are neglected in the theory since a symmetric bubble is assumed.

Since the data points were obtained around parameters in which beam loading generates quasi-monoenergetic electron bunches, the first factor is likely the main reason for this observation.

The data shown in figure 4 indicate that it is possible that all electrons within the bubble can execute the same bubbletron motion if the potential is symmetric. From figure 4(c), a few oscillations can be expected above $\gamma > 100$ where most x-ray photons are emitted as synchrotron radiation. Therefore, in order to accommodate many transverse oscillations like ‘betatron’ motion, a spherical bubble shape is not ideal but rather an elongated cylindrical shape may be preferable such that the observed motion could approach that described in the betatron model. This elongation could be expected when beam loading is strong enough to change the shape of the bubble [40]. After this elongation, the injection point of electron moves backward and consequently the distance between the head of the bubble and the injection point increases. However, the E_z field becomes weaker due to beam loading which might result in a somewhat lower electron energy compared with no loading.

The observed effect of the increasing beam divergence with bunch charge suggests a trade off between photon number (photon energy) and beam divergence (possibly source size) for generating bright x-ray beams. Increasing bunch charge yields a larger number of photons and a larger beam divergence and also hence a large number of energetic photons due to increased r_b .

4. Conclusions

In conclusion, our experiments have shown evidence for three regimes of electron injection for LWFA experiments. These include injection of a single bunch, multiple consecutive injection events of electron bunches into the wakefield and injection of a high current beam, which was susceptible to break up within the bubble due to asymmetries in the wakefield. Multiple injections were observed at plasma densities above a threshold where beam loading is effective. In addition an analytical formula for the ‘bubbletron’ model shows reasonable agreement with the experimental data in describing the transverse motion in the bubble, within the limitations of the model. The RMS electron beam divergence was found to increase with bunch charge and likely resulted from beam loading affecting the injection process into the bubble.

Acknowledgments

This work was supported by the US National Science Foundation through the Physics Frontier Center FOCUS grant no. PHY-0114336, NSF/DNDO grant no. 0833499 and NSF CAREER grant no. PHY-1054164.

References

- [1] Tajima T and Dawson J M 1979 *Phys. Rev. Lett.* **43** 267
- [2] Mangles S P D *et al* 2004 *Nature* **431** 535
- [3] Geddes C G R *et al* 2004 *Nature* **431** 538
- [4] Faure J *et al* 2004 *Nature* **431** 541
- [5] Leemans W P, Nagler B, Gonsalves A J, Tóth Cs, Nakamura K, Geddes C G R, Esarey E, Schroeder C B and Hooker S M 2006 *Nat. Phys.* **2** 696
- [6] Maksimchuk A *et al* 2008 *Phys. Plasmas* **15** 056703
- [7] Hafz N A M *et al* 2008 *Nature Photonics* **2** 571
- [8] Wang H *et al* 2012 *Nature Commun.* **4** 1988
- [9] Kim H T *et al* 2013 *Phys. Rev. Lett.* **111** 165002
- [10] de Frank G 2001 *Chem. Rev.* **101** 1779
- [11] Parsons J G *et al* 2002 *Appl. Spectrosc. Rev.* **37** 187
- [12] Baker S H *et al* 2009 *J. Phys.: Condens. Matter* **21** 183002
- [13] Rousse A *et al* 2004 *Phys. Rev. Lett.* **93** 135005
- [14] Phuoc K T *et al* 2005 *Phys. Plasmas* **12** 023101
- [15] Shah R *et al* 2006 *Phys. Rev. E* **74** 045401
- [16] Albert F *et al* 2008 *Phys. Rev. E* **77** 056402
- [17] Thomas A G R and Krushelnick K 2009 *Phys. Plasmas* **16** 103103
- [18] Fourmaux S *et al* 2011 *New J. Phys.* **13** 033017
- [19] Corde S, Ta Phuoc K, Lambert G, Fitour R, Malka V and Rousse A 2013 *Rev. Mod. Phys.* **85** 1–48
- [20] Kneip S *et al* 2008 *Phys. Rev. Lett.* **100** 105006-1
- [21] Kneip S *et al* 2010 *Nature Phys.* **6** 980
- [22] Plateau G R *et al* 2012 *Phys. Rev. Lett.* **109** 064802
- [23] Kostyukov *et al* 2003 *Phys. Plasmas* **10** 4818–28
- [24] Esarey E *et al* 2002 *Phys. Rev. E* **65** 056505
- [25] Mangles S P D *et al* 2009 *Appl. Phys. Lett.* **95** 181106
- [26] Cummings P and Thomas A G R 2011 *Phys. Plasmas* **18** 053110
- [27] Schnell M *et al* 2013 *Nature Commun.* **4** 2421
- [28] Pukhov A and Meyer-ter-vehn J 2002 *Appl. Phys. B* **74** 355
- [29] Kostyukov *et al* 2004 Phenomenological theory of laser-plasma interaction in ‘bubble’ regime *Phys. Plasmas* **11** 5256
- [30] Lu W, Tzoufras M, Joshi C, Tsung F S, Mori W B, Vieira J, Fonseca R A and Silva L O 2007 *Phys. Rev. ST Accel. Beams* **10** 061301
- [31] Semushin S and Malka V 2001 *Rev. Sci. Instrum.* **72** 7
- [32] Bahk S W *et al* 2004 *Opt. Lett.* **29** 2837
- [33] Tanaka K A *et al* 2005 *Rev. Sci. Instrum.* **76** 013507
- [34] Froula D H *et al* 2009 *Phys. Rev. Lett.* **103** 215006
- 2012 *Phys. Rev. ST Accel. Beams* **15** 011302
- McGuffey C *et al* 2012 *Phys. Plasmas* **19** 063113
- [35] Vargas M *et al* 2012 *AIP Conf. Proc.* **1507** 336
- [36] Glinec Y *et al* 2008 *Eur. Phys. Lett.* 64001
- [37] Popp A *et al* 2010 *Phys. Rev. Lett.* **105** 215001
- [38] Kotaki H *et al* 2011 *Plasma Phys. Control. Fusion* **53** 014009
- [39] Matsuoka T *et al* 2009 *Proc. the 2nd Int. Symp. On Laser-Driven Relativistic Plasmas Applied to Science, Industry and Medicine (Kyoto, 2009) (AIP Conf. Proc.)* p 182
- [40] Tzoufras M *et al* 2008 *Phys. Rev. Lett.* **101** 145002
- [41] Dong P *et al* 2010 *Phys. Rev. Lett.* **104** 134801
- [42] Kostyukov I, Nerush E, Pukhov A and Seredov V 2009 *Phys. Rev. Lett.* **103** 175003
- [43] Thomas A G R 2010 *Phys. Plasmas* **17** 056708
- [44] Decker C D, Mori W B, Tzeng K-C and Katsouleas T 1996 *Phys. Plasmas* **3** 2047
- [45] Matsuoka T *et al* 2010 *Phys. Rev. Lett.* **105** 034801
- [46] Debus A D *et al* 2010 *Phys. Rev. Lett.* **104** 084802
- [47] Mangles S P D 2006 *Phys. Rev. Lett.* **96** 215001